Progress In Electromagnetics Research, PIER 72, 307–323, 2007

PHASE-MATCHING THE HYBRID FV24/S22 FDTD ALGORITHM

M. F. Hadi

Electrical Engineering
Kuwait University
P.O. Box 5969, Safat 13060, Kuwait

R. K. Dib

College of Technological Studies
Public Authority of Applied Education and Training
P.O. Box 4196, Hawalli 32072, Kuwait

Abstract—This work demonstrates an efficient and simple approach for applying high-order extended-stencil FDTD algorithms near planar perfect electric conductors (PEC) boundaries while minimizing spurious reflections off the interface between the high-order grid and the mandated special compact cells around PEC boundaries. This proposed approach eliminates the need for cumbersome subgridding implementations and provides a superior alternative in minimizing spurious reflections without any added modeling complexity or computing costs. The high-order algorithm used in this work is the recently proposed three-dimensional FV24 algorithm and the proposed approach can be easily extended to the standard Fang high-order FDTD algorithm which represents a special case of the highly phase-coherent FV24 algorithm.

1. INTRODUCTION

Several FDTD algorithms have been developed over the past decade to minimize the loss of phase coherence in wave solutions due to numerical dispersion. Shlager and Schneider [1] compared some of the more prominent low-dispersion algorithms and compared their phase coherence in both single-frequency and wideband applications. While some of the analyzed algorithms that restricted their stencils to a single Yee cell did extremely well in single-frequency applications [2, 3], it was

the two-dimensional extended-stencil M24 algorithm [4] that excelled in wideband suitability. Since its introduction two attempts were made in the past to extend the M24 algorithm to 3D space [5, 6]. However, it was only recently made possible in a way that preserved the M24's superior phase coherence in single-frequency applications while maintaining its wideband applicability [7]. This new algorithm was based on a finite-volumes approach and was named the FV24 algorithm.

The main challenge to the extended-stencil M24 and FV24 algorithms, however, is porting the wealth of FDTD tools (e.g., recent advances in PML design [8] and FDTD parallel coding [9]) that were developed over the decades for the standard single-cell Yee scheme (S_{22} for second-order differencing in both time and space). It was suggested in [4] that this challenge could be simply resolved by introducing minimal S_{22} buffer zones where needed in an otherwise global M24 (or FV24) implementation. Haussmann in [5], however, demonstrated experimentally that such an approach would cause measurable reflections at the interface between the high-order and low-order subdomains of the FDTD lattice. Another approach was demonstrated by Georgakopoulos et al. and Abd El-Raouf et al. [10, 11] in using a fine-meshed S_{22} buffer zone against a globally fourth-order domain. There too spurious reflections were possible if extra care was not taken to ensure exact phase velocity matching between the coarsely-meshed and finely-meshed FDTD lattice subdomains as demonstrated by Celuch-Marcysiak and Rudnicki [12]. The common cause of spurious reflections in both hybrid high-order/low-order approaches was recently investigated and effectively cured by Hadi and Dib [13] for the two-dimensional hybrid M24/S_{22} algorithm. This approach will be further developed and extended in the present work to the more challenging three-dimensional hybrid FV24/S_{22} algorithm, by analyzing the spurious reflections off the planar FDTD lattice interfaces and developing special algorithm modifications to eliminate these phase mismatch-borne anomalies.

2. REVIEW OF THE FV24 ALGORITHM

This algorithm is the natural 3D extension to the 2D high-order M24 algorithm. Whereas the M24 update equations were derived from concentric loop integrals around the field node of interest, the FV24 update equations are derived from concentric surface integrals. For example, the update equation for an E_x field node would be

$$\frac{\epsilon}{\Delta t}\left[E_x|^{n+\frac{1}{2}} - E_x|^{n-\frac{1}{2}}\right] = D_y H_z - D_z H_y, \tag{1}$$

where D_y and D_z are difference operators that represent weighted contributions of the field nodes occupying the surrounding concentric surfaces shown in Fig. 1. Expanding the operator D_y as an example we get

$$D_y = K_a D_y^a + K_b D_y^b + K_c D_y^c + K_d D_y^d \tag{2}$$

with

$$D_y^a H_z = \frac{1}{h}\left[H_z|_{j+\frac{1}{2}} - H_z|_{j-\frac{1}{2}}\right] \tag{3}$$

$$D_y^b H_z = \frac{1}{3h}\left[H_z|_{j+\frac{3}{2}} - H_z|_{j-\frac{3}{2}}\right] \tag{4}$$

$$D_y^c H_z = \frac{1}{12h}\begin{bmatrix} H_z|_{i+1,j+\frac{3}{2}} + H_z|_{i-1,j+\frac{3}{2}} \\ +H_z|_{j+\frac{3}{2},k+1} + H_z|_{j+\frac{3}{2},k-1} \\ -H_z|_{i+1,j-\frac{3}{2}} - H_z|_{i-1,j-\frac{3}{2}} \\ -H_z|_{j-\frac{3}{2},k+1} - H_z|_{j-\frac{3}{2},k-1} \end{bmatrix} \tag{5}$$

$$D_y^d H_z = \frac{1}{12h}\begin{bmatrix} H_z|_{i+1,j+\frac{3}{2},k+1} + H_z|_{i-1,j+\frac{3}{2},k+1} \\ +H_z|_{i+1,j+\frac{3}{2},k-1} + H_z|_{i-1,j+\frac{3}{2},k-1} \\ -H_z|_{i+1,j-\frac{3}{2},k+1} - H_z|_{i-1,j-\frac{3}{2},k+1} \\ -H_z|_{i+1,j-\frac{3}{2},k-1} - H_z|_{i-1,j-\frac{3}{2},k-1} \end{bmatrix}, \tag{6}$$

where the non-staggered i, j, k and n indices are omitted for cleaner notation and $K_a = 1 - K_b - K_c - K_d$.

Following the example of Taflove [14] by inserting plane wave trial solutions into the resulting update equations the difference operators can be transformed into the discrete operators

$$D_t = \jmath \frac{\sin\frac{\omega\Delta t}{2}}{\Delta t/2} \tag{7}$$

and

$$D_x = \jmath K_a \frac{\sin\frac{\beta_x h}{2}}{h/2} + \jmath \frac{\sin\frac{3\beta_x h}{2}}{3h/2} \cdot \left(K_b + \frac{K_c}{2}(\cos\beta_y h + \cos\beta_z h) + K_d \cos\beta_y h \cos\beta_z h\right) \tag{8}$$

$$D_y = \jmath K_a \frac{\sin\frac{\beta_y h}{2}}{h/2} + \jmath \frac{\sin\frac{3\beta_y h}{2}}{3h/2} \cdot \left(K_b + \frac{K_c}{2}(\cos\beta_x h + \cos\beta_z h) + K_d \cos\beta_x h \cos\beta_z h\right) \tag{9}$$

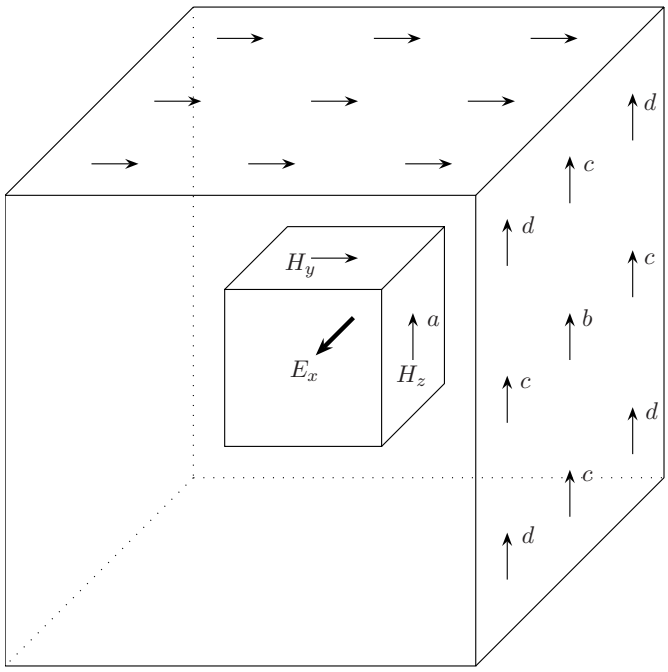

Figure 1. The concentric enclosing surfaces of an FV24 cell around an E_x component (an h^3 inner volume within an extended $(3h)^3$ volume). Small letter designations are repetitive on each of the 4 sides and correspond to the weighted H-field groupings in the FV24 update equation. A uniform $\Delta x = \Delta y = \Delta z = h$ is assumed.

$$D_z = \jmath K_a \frac{\sin\frac{\beta_z h}{2}}{h/2} + \jmath \frac{\sin\frac{3\beta_z h}{2}}{3h/2} \cdot \left(K_b + \frac{K_c}{2}(\cos\beta_x h + \cos\beta_y h) + K_d \cos\beta_x h \cos\beta_y h \right), \quad (10)$$

where $\jmath = \sqrt{-1}$. The dispersion relation of the resulting algorithm can be concisely written using (7)–(10) as [5]

$$\mu\epsilon D_t^2 = D_x^2 + D_y^2 + D_z^2 \quad (11)$$

and the stability criterion as

$$\Delta t \leq \frac{2\sqrt{\mu\epsilon}}{\sqrt{(D_x^2 + D_y^2 + D_z^2)_{\max}}} = \frac{h}{c\sqrt{3}} \frac{3}{|3 - 4K_b - 2K_c - 4K_d|}. \quad (12)$$

Table 1. Optimum K-values for the FV24 algorithm at different resolution factors.

R	K_b	K_c	K_d
5	−0.132595513	−0.034455612	0.057380229
10	−0.108982724	−0.024711001	0.038444028
15	−0.105291887	−0.023367479	0.035822568
20	−0.104042707	−0.022923377	0.034956192
25	−0.103471738	−0.022722165	0.034563713
30	−0.103163470	−0.022613994	0.034352733
35	−0.102978234	−0.022549148	0.034226265

To complete the FV24 algorithm appropriate values for the weighting parameters K_b, K_c and K_d need to be found with the aim of optimizing phase coherence of the algorithm's wave solutions. Table 1 lists such values for a range of FDTD resolution factors [7].

It is worth noting here that the specific choices $K_b = -1/8$, $K_c = K_d = 0$ will produce Fang's high-order S_{24} algorithm [15] whereas the choices $K_b = K_c = K_d = 0$ will produce Yee's S_{22} algorithm. The clear advantage of the M24 and FV24 high-order algorithms can be evidenced by the direct and computationally efficient modeling of wave propagation in buildings [4], compared to the indirect or frequency-limited approaches (e.g., [17]) mandated by the prohibitively huge computational demands of the standard FDTD algorithm when modeling electrically large structures.

3. NUMERICAL REFLECTION ANALYSIS

A straightforward hybrid FV24/S_{22} implementation would constitute a global FV24 algorithm application on a standard FDTD gird that is punctuated by minimal S_{22} subdomains. In such subdomains where the extended-stencil FV24 implementation is either inconvenient or impossible, the modeling task is delegated to the compact S_{22} algorithm. Due to the incompatible numerical dispersion behavior of the two mated algorithms, however, spurious reflections are expected at the common interface.

Let us consider the planar interface demonstrated in Fig. 2 between two zones in a homogeneous FDTD lattice in which the left zone field nodes are updated using the FV24 algorithm and the right

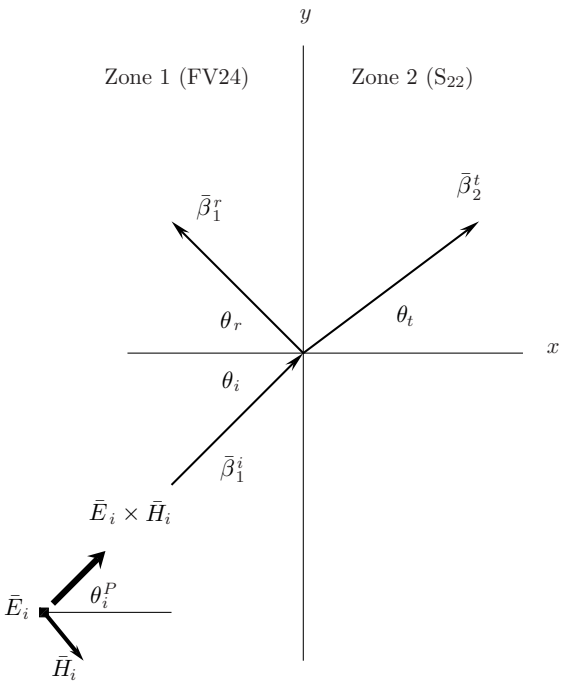

Figure 2. Interpretation of a plane wave interaction with a planar interface separating two similarly gridded homogeneous zones with different FDTD schemes. Field nodes on the y-axis are assumed part of zone 2.

zone field nodes (including those lying on the planar interface) are updated using the S_{22} algorithm. It has been shown in [13] that such FDTD algorithm inhomogeneity will manifest itself in the form of spurious reflections off the planar interface. For the particular geometry of Fig. 2 these spurious reflections could be accurately predicted using

$$\Gamma = \frac{1-\kappa}{1+\kappa} \qquad \text{with} \qquad \kappa = \frac{\cos\theta_t^P \cos\dfrac{\beta_{2x}h}{2}}{\cos\theta_i^P \cos\dfrac{\beta_{1x}h}{2}}. \tag{13}$$

For any wave incidence angle θ_i the numerical phase velocity components β_{1x} and β_{1y} could be calculated from the left-zone dispersion relation. The right-zone dispersion relation is then used to

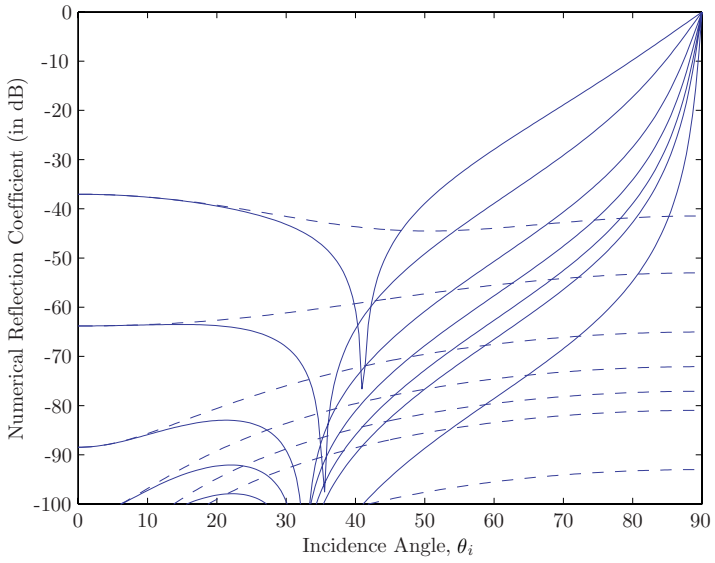

Figure 3. Numerical reflection coefficient vs. θ_i across an FV24/S_{22} hybrid algorithm interface parallel to the xy–plane before (solid) and after (dashed) modification at the resolution factors (from top to bottom) $R = 5, 10, 20, 30, 40, 50, 100$.

calculate β_{2x} and θ_t after enforcing the boundary condition $\beta_{2y} = \beta_{1y}$. The incident and transmitted wave vectors' polarization angles are then calculated from

$$\theta_i^P = \tan^{-1} \left. \frac{D_y}{D_x} \right|_{\text{zone 1}} \quad \text{and} \quad \theta_t^P = \tan^{-1} \left. \frac{D_y}{D_x} \right|_{\text{zone 2}}, \tag{14}$$

where D_x and D_y are given by (8)–(9) for zone 1 and by

$$D_x = \jmath \frac{\sin \frac{\beta_x h}{2}}{h/2} \quad \text{and} \quad D_y = \jmath \frac{\sin \frac{\beta_y h}{2}}{h/2} \tag{15}$$

for zone 2, and finally, the numerical reflection coefficient is evaluated using (13). Fig. 3 illustrates this numerical reflection variation vs. the wave incidence angle at different resolution factors (solid lines). For every resolution factor the numerical reflection always degenerate to total reflection as the incidence angle approaches $\pi/2$, which would cause severe distortions to the hybrid algorithm's wave solutions.

For this disruptive reflection to be eliminated both joined algorithms must have precisely matched dispersion characteristics

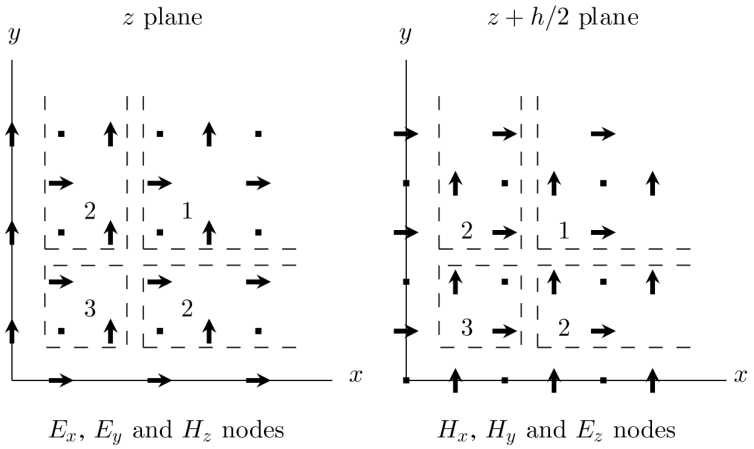

Figure 4. An FDTD lattice near a PEC edge extending along the z-axis. The three different subdomain regions require three different sets of update equations.

within the common interface. Fig. 4 illustrates a classic challenging situation where reliable update equations are desired near perfectly conducting boundaries. The two grids of the figure represent consecutive cuts along the z-axis. While the extended-stencil FV24 algorithm could be freely implemented within the interior Region 1 subdomain, special update equations are required for the planar Region 2 and axial (spinal) Region 3 subdomains. Furthermore, these update equations must be drafted such that their tangential dispersion characteristics are precisely matched across each of the subdomain two-dimensional interfaces.

4. PHASE-MATCHING AT PLANAR BOUNDARIES

An appropriate set of phase-matched update equations for a Region 2 subdomain parallel to the yz-plane can be written with the help of Fig. 5 as

$$\begin{aligned}\epsilon\frac{\partial E_x}{\partial t} &= \frac{K_b^b}{3h}\left(H_z|_{j+\frac{3}{2}} - H_z|_{j-\frac{3}{2}} - H_y|_{k+\frac{3}{2}} + H_y|_{k-\frac{3}{2}}\right) \\ &\quad + \frac{K_c^b}{6h}\begin{pmatrix} H_z|_{j+\frac{3}{2},k-1} + H_z|_{j+\frac{3}{2},k+1} \\ -H_z|_{j-\frac{3}{2},k-1} - H_z|_{j-\frac{3}{2},k+1} \\ -H_y|_{j-1,k+\frac{3}{2}} - H_y|_{j+1,k+\frac{3}{2}} \\ +H_y|_{j-1,k-\frac{3}{2}} + H_y|_{j+1,k-\frac{3}{2}} \end{pmatrix}\end{aligned}$$

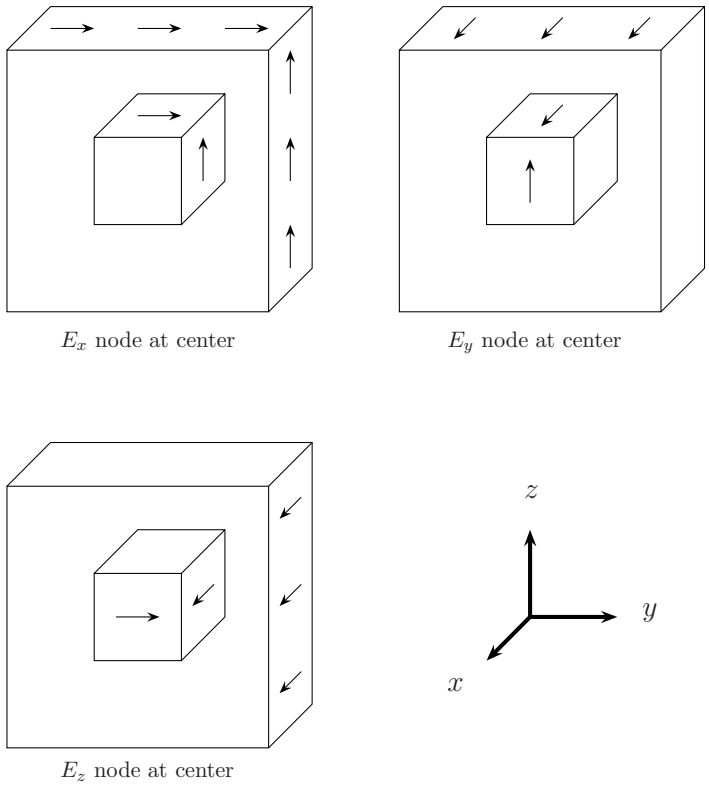

Figure 5. Surrounding H nodes used for E_x, E_y and E_z update equations (16)–(18) for an yz-plane-parallel Region 2 subdomain.

$$\begin{aligned} & + \frac{K_a^b}{h} \begin{pmatrix} H_z|_{j+\frac{1}{2}} - H_z|_{j-\frac{1}{2}} \\ -H_y|_{k+\frac{1}{2}} + H_y|_{k-\frac{1}{2}} \end{pmatrix} \qquad (16) \\ \epsilon \frac{\partial E_y}{\partial t} &= \frac{H_z|_{i-\frac{1}{2}} - H_z|_{i+\frac{1}{2}}}{h} + \frac{K_b^b}{3h} \left(H_x|_{k+\frac{3}{2}} - H_x|_{k-\frac{3}{2}} \right) \\ & + \frac{K_c^b}{6h} \begin{pmatrix} H_x|_{j-1,k+\frac{3}{2}} + H_x|_{j+1,k+\frac{3}{2}} \\ -H_x|_{j-1,k-\frac{3}{2}} - H_x|_{j+1,k-\frac{3}{2}} \end{pmatrix} \\ & + \frac{K_a^b}{h} \left(H_x|_{k+\frac{1}{2}} - H_x|_{k-\frac{1}{2}} \right) \qquad (17) \\ \epsilon \frac{\partial E_z}{\partial t} &= \frac{H_y|_{i+\frac{1}{2}} - H_y|_{i-\frac{1}{2}}}{h} + \frac{K_b^b}{3h} \left(H_x|_{j-\frac{3}{2}} - H_x|_{j+\frac{3}{2}} \right) \end{aligned}$$

$$+\frac{K_c^b}{6h}\begin{pmatrix} H_x|_{j-\frac{3}{2},k-1} + H_x|_{j-\frac{3}{2},k+1} \\ -H_x|_{j+\frac{3}{2},k-1} - H_x|_{j+\frac{3}{2},k+1} \end{pmatrix}$$
$$+\frac{K_a^b}{h}\left(H_x|_{j-\frac{1}{2}} - H_x|_{j+\frac{1}{2}}\right) \tag{18}$$

with $K_a^b = 1 - K_b^b - K_c^b$. The update equations for the H-field components can be written from the above with the direct substitutions $\epsilon \to -\mu$, $E \to H$ and $H \to E$ while leaving all indices, subscripts and coefficients untouched. The update equations for the xy and xz-planes can be similarly derived. Key features of the above update equations are

(i) Stencil extension along the normal x-axis is limited to one FDTD cell preventing its encroaching beyond the PEC boundary.

(ii) The selection of the included field nodes is carefully tailored to allow perfect tangential phase-matching with simple and logical choices of the weighting K^b parameters.

The corresponding discrete operators of the above special update equations are

$$D_x = \jmath \frac{\sin\dfrac{\beta_x h}{2}}{h/2} \tag{19}$$

$$D_y = \jmath K_a^b \frac{\sin\dfrac{\beta_y h}{2}}{h/2} + \jmath\left(K_b^b + K_c^b \cos\beta_z h\right)\frac{\sin\dfrac{3\beta_y h}{2}}{3h/2} \tag{20}$$

$$D_z = \jmath K_a^b \frac{\sin\dfrac{\beta_z h}{2}}{h/2} + \jmath\left(K_b^b + K_c^b \cos\beta_y h\right)\frac{\sin\dfrac{3\beta_z h}{2}}{3h/2}, \tag{21}$$

with the dispersion relation obtainable from (11) and the stability criterion governed by[†]

$$\Delta t \le \frac{h}{c}\frac{1}{\sqrt{1 + 2\left(1 - 4K_b^b/3 - 2K_c^b/3\right)^2}}. \tag{22}$$

To determine the appropriate K^b-values for perfect phase-matching at the yz-planar interface, the FV24 discrete operators (9)–

[†] The eventual choices of $K_{b,c}^b$ will maintain the stability criterion (12) fully contained within (22) for all resolution factors of Table 1, ensuring overall algorithm stability when the chosen time step is based on (12).

(10) are re-written as $\beta_x \to 0$,

$$D_y = \jmath K_a \frac{\sin\frac{\beta_y h}{2}}{h/2} + \jmath \frac{\sin\frac{3\beta_y h}{2}}{3h/2} \cdot \left[K_b + \frac{K_c}{2} + \left(\frac{K_c}{2} + K_d\right)\cos\beta_z h\right] \quad (23)$$

$$D_z = \jmath K_a \frac{\sin\frac{\beta_z h}{2}}{h/2} + \jmath \frac{\sin\frac{3\beta_z h}{2}}{3h/2} \cdot \left[K_b + \frac{K_c}{2} + \left(\frac{K_c}{2} + K_d\right)\cos\beta_y h\right] \quad (24)$$

and compared to (20)–(21) which would readily yield

$$K_b^b = K_b + \frac{K_c}{2} \quad \text{and} \quad K_c^b = K_d + \frac{K_c}{2}. \quad (25)$$

Fig. 3 compares the post-phase-matching reflections (dashed lines) with the FV24/S_{22} reflections discussed earlier, clearly demonstrating the advantage of tangential dispersion matching across such planar interfaces. The only remaining (and relatively tame) cause of numerical reflections is the jump in stencil depth along the normal direction from three-cells to one-cell depth.

5. PHASE-MATCHING AT AXIAL EDGES

Taking the z-axial edge and the corresponding Region 3 of Fig. 4 as an example, an appropriate set of update equations that would have one-cell stencil depth along both x and y-axes while maintaining a three-cells stencil depth along the z-axis would be

$$\epsilon\frac{\partial E_x}{\partial t} = \frac{H_z|_{j+\frac{1}{2}} - H_z|_{j-\frac{1}{2}}}{h} + \frac{1-K^e}{h}\left(H_y|_{k-\frac{1}{2}} - H_y|_{k+\frac{1}{2}}\right) + \frac{K^e}{3h}\left(H_y|_{k-\frac{3}{2}} - H_y|_{k+\frac{3}{2}}\right) \quad (26)$$

$$\epsilon\frac{\partial E_y}{\partial t} = \frac{H_z|_{i-\frac{1}{2}} - H_z|_{i+\frac{1}{2}}}{h} + \frac{1-K^e}{h}\left(H_x|_{k+\frac{1}{2}} - H_x|_{k-\frac{1}{2}}\right) + \frac{K^e}{3h}\left(H_x|_{k+\frac{3}{2}} - H_x|_{k-\frac{3}{2}}\right) \quad (27)$$

$$\epsilon\frac{\partial E_z}{\partial t} = \frac{H_y|_{i+\frac{1}{2}} - H_y|_{i-\frac{1}{2}} - H_x|_{j+\frac{1}{2}} + H_x|_{j-\frac{1}{2}}}{h} \quad (28)$$

with matching H-components update equations. The corresponding discrete operators would be

$$D_x = \jmath \frac{\sin \dfrac{\beta_x h}{2}}{h/2} \tag{29}$$

$$D_y = \jmath \frac{\sin \dfrac{\beta_y h}{2}}{h/2} \tag{30}$$

$$D_z = \jmath(1 - K^e) \frac{\sin \dfrac{\beta_z h}{2}}{h/2} + \jmath K^e \frac{\sin \dfrac{3\beta_z h}{2}}{3h/2}. \tag{31}$$

Following the example of the previous section by comparing the above D_z discrete operator with those of the adjacent Region 1 or Region 2 of Fig. 4 after setting the limits $\beta_x \to 0$ and $\beta_y \to 0$ we can deduce the simple phase-matching condition

$$K^e = K_b^b + K_c^b = K_b + K_c + K_d. \tag{32}$$

The update equations and discrete operators of the x and y-axial subdomains would provide the same condition.

The analysis and derived update equations modifications of this section and the last can be straightforwardly applied towards the hybrid three-dimensional S_{24}/S_{22} algorithm by simply setting $K_b = -1/8$ and $K_c = K_d = 0$.

6. NUMERICAL VALIDATION

To validate the proposed hybrid $FV24/S_{22}$ phase-matching, an extreme yet simple test is chosen in the form of a 3D metallic resonator. The resonator walls are made of perfect conductors with dimensions $\lambda \times \lambda \times 10\lambda$. The FDTD resolution factor used is $R = 10$ cells/λ and the Gaussian input signal is injected at the location $(\lambda/2, \lambda/2, \lambda/2)$ with the measuring probe at the opposite symmetrical end of the long resonator. Such a structure will serve our purposes well since it provides relatively large interface surfaces for the volume. It also furnishes a large number of reflections, especially at steep incidence angles to compound and highlight any generated spurious reflections.

Fig. 6 compares several $FV24/S_{22}$ hybrid variants to the benchmark S_{22} results in terms of the critical criterion of maintaining non-growing resonance levels as time marches on. From the figure the worst performing variant is the straight hybridding with no attempted

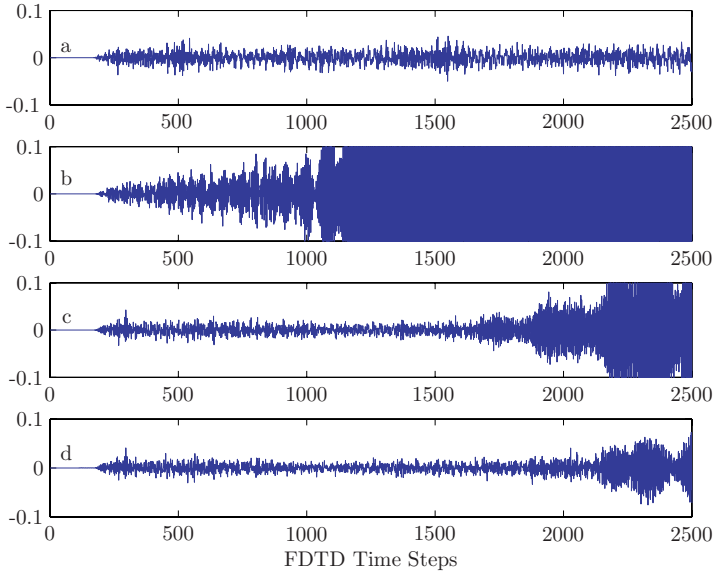

Figure 6. Resonator probe signal (E_z) for the FDTD algorithm variants: a) S_{22}, b) FV24/S_{22} with no phase-matching, c) FV24/S_{22} with planar phase-matching, d) FV24/S_{22} with both planar and axial edges phase-matching. Resonator input was a band-limited Gaussian pulse.

phase-matching (Fig. 6b), where the field solution (at the probe) starts growing almost immediately, and uncontrollably so beginning at the time index $n = 1,000$. In comparison, the proposed phase matching at the planar and axial hybrid algorithm interfaces helped maintain non-growing field solutions till beyond $n = 2,000$ time steps which corresponds to approximately 10 full reflection-intensive traversings of the entire length of the metallic resonator (Fig. 6d). Fig. 6c demonstrates the negative effect of omitting phase-matching along the axial edges. Eventually, however, even the tame interface reflections due to the normal-direction phase mismatches will accumulate large enough levels to start disrupting the collected data in this extreme test.

To verify the accuracy of the phase-matched hybrid FV24/S_{22} algorithm in predicting the resonator modes, Fig. 7 displays the FFT responses of the collected E_z data (dashed curves) based on 2,048 time steps for the hybrid FV24/S_{22} and S_{22} algorithms. Although the data series is short by FFT standards the hybrid algorithm managed to keep

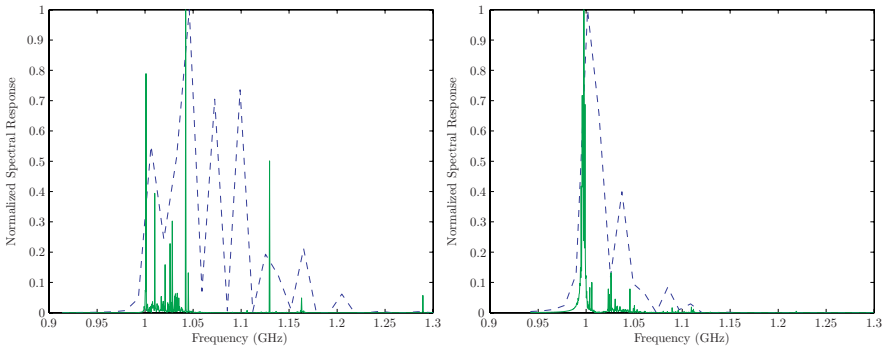

Figure 7. Spectral response of the phase-matched FV24/S_{22} (left) and S_{22} (right) algorithms. Dashed curves: FFT based on 2,048 time steps. Solid curves: Frequency resolution enhancement based on 31 FFT data points and a 15th order diagonal Padé interpolant.

track of more resonance modes than the S_{22} algorithm, mainly due to the former's inherent superior phase coherence. Fig. 7 also displays higher resolution spectral responses (solid curves) that were obtained using Dey and Mittra's Padé-on-FFT approach [16] which basically applies a Padé rational function approximation [18] on a coarse FFT output with the objective of boosting its frequency resolution. In this case 31 FFT data points were used in conjunction with a 15th order diagonal Padé approximation[‡]. The resulting interpolations clearly demonstrate the dispersive nature of the regular FDTD (S_{22}) algorithm when attempting to model electrically large structures using a coarse wavelength resolution—an inherent shortcoming that the FV24 algorithm was specifically designed to overcome.

7. CONCLUSION

The one major obstacle standing in the way of wide adoption of high-order FDTD algorithms has always been the difficulty in dealing with perfectly conducting boundaries. Until recently the work-around solution has been using cumbersome subgridding techniques within low-order FDTD buffer layers around PEC objects, where the low order layers are meant to guard against FDTD cell enchroachment beyond the PEC boundaries and the subgridding is meant for a rough

[‡] Higher Padé orders will allow detecting more resonance modes as desired. It would be a futile exercise here though since the odd resonator dimensions produces many closely packed modes.

matching technique between the high-order and low-order zones.

Recently, however, the very cause of FDTD hybrid interface mismatches has been investigated and quantified for two-dimensional implementations—namely, the differences in normal and tangential numerically rendered phase velocities across the interface as dictated by the respective dispersion relations. It was found that while normal phase mismatches are relatively benign, tangential mismatches on the other hand are serious contributors to FDTD solution errors. To eliminate these tangential mismatches, the idea of mixed differencing operators within the same update equation as a simpler and superior substitute to subgridding was introduced and applied to the two dimensional hybrid $M24/S_{22}$ algorithm.

In this work, these analysis were carried over and applied to the more challenging three dimensional hybrid $FV24/S_{22}$ algorithm. Special phase-matching modifications to the buffer layers' update equations were proposed and experimentally validated, which unlike in the $M24/S_{22}$ case, did not require the extra step of calculating specially optimized weighting parameters. The proposed modifications could be easily applied to the hybrid S_{24}/S_{22} algorithm with a simple K-parameters substitution and the methodology could be easily adapted to other hybrid high-order/low-order FDTD variants.

REFERENCES

1. Shlager, K. L. and J. B. Schneider, "Comparison of the dispersion properties of several low-dispersion finite-difference time-domain algorithms," *IEEE Trans. Antennas Propagat.*, Vol. 51, No. 3, 642–653, Mar. 2003.
2. Forgy, E. A. and W. C. Chew, "A time-domain method with isotropic dispersion and increased stability on an overlapped lattice," *IEEE Trans. Antennas Propagat.*, Vol. 50, No. 7, 983–996, July 2002.
3. Cole, J. B., "A high-accuracy realization of the Yee algorithm using non-standard finite differences," *IEEE Trans. Microwave Theory Tech.*, Vol. 45, No. 6, 991–996, June 1997.
4. Hadi, M. F. and M. Piket-May, "A modified FDTD (2,4) scheme for modeling electrically large structures with high-phase accuracy," *IEEE Trans. Antennas Propagat.*, Vol. 45, No. 2, 254–264, Feb. 1997.
5. Haussmann, G. J., "A dispersion optimized three-dimensional finite-difference time-domain method for electromagnetic analy-

sis," Ph.D. dissertation, University of Colorado at Boulder, Boulder, CO, 1998.

6. Abd El-Raouf, H. E., E. A. El-Diwani, A. Ammar, and F. El-Hefnawi, "A low-dispersion 3-D second-order in time fourth-order in space FDTD scheme ($m3d_{24}$)," *IEEE Trans. Antennas Propagat.*, Vol. 52, No. 7, 1638–1646, July 2004.
7. Hadi, M. F., "A super-phase coherent 3d high-order FDTD algorithm," *23rd International Review of Progress in Applied Computational Electromagnetics*, Verona, Italy, Mar. 2007.
8. Shi, Y. and C. H. Liang, "A strongly well-posed PML with unsplit-field formulations in cylindrical and spherical coordinates," *Journal of Electromagnetic Waves and Applications*, Vol. 19, No. 13, 1761–1776, 2005.
9. Zhang, Y., W. Ding, and C. H. Liang, "Study on the optimum virtual topology for MPI based parallel conformal FDTD algorithms on PC clusters," *Journal of Electromagnetic Waves and Applications*, Vol. 19, No. 13, 1817–1831, 2005.
10. Georgakopoulos, S. V., C. R. Birtcher, C. A. Balanis, and R. A. Renaut, "HIRF penetration and PED coupling analysis for scaled fuslage models using a hybrid subgrid FDTD(2,2)/FDTD(2,4) method," *IEEE Trans. Electromagn. Compat.*, Vol. 45, No. 2, 293–305, May 2003.
11. Abd El-Raouf, H. E., E. A. El-Diwani, A. E.-H. Ammar, and F. M. El-Hefnawi, "A FDTD hybrid "$m3d$24-yee" scheme with subgridding for solving large electromagnetic problems," *Appl. Computat. Electromagn. Soc. J.*, Vol. 17, No. 1, 23–29, Mar. 2002.
12. Celuch-Marcysiak, M. and J. Rudnicki, "A study of numerical reflections caused by fdtd mesh refinements in 1d and 2d," *15th Ann. Conf. Microwave Radar Wireless Comm.*, 626–629, Warsaw, Poland, May 2004.
13. Hadi, M. F. and R. K. Dib, "Phase-matching the hybrid m24/s22 fdtd algorithm," *23rd International Review of Progress in Applied Computational Electromagnetics*, Verona, Italy, Mar. 2007.
14. Taflove, A., *Computational Electrodynamics: The Finite-Difference Time-Domain Method*, Artech House, Boston, MA, 1995.
15. Fang, J., "Time domain finite difference computation for Maxwell's equations," Ph.D. dissertation, University of California at Berkeley, Berkeley, CA, 1989.

16. Dey, S. and R. Mittra, "Efficient computation of resonant frequencies and quality factors of cavities via a combination of the finite-difference time-domain technique and the Padé approximation," *IEEE Microwave Guided Wave Lett.*, Vol. 8, No. 12, 415–417, Dec. 1998.
17. Golestani-Rad, L., J. Rashed-Mohassel, and M. M. Danaie, "Rigorous analysis of EM-wave penetration into a typical room using FDTD method: the transfer function concept," *Journal of Electromagnetic Waves and Applications*, Vol. 20, No. 7, 913–926, 2006.
18. Ojeda, X. and L. Pichon, "Combining the finite element method and a Pade approximation for scattering analysis application to radiated electromagnetic compatibility problems," *Journal of Electromagnetic Waves and Applications*, Vol. 19, No. 10, 1375–1390, 2005.